The engineering properties and reaction mechanism of MgO-activated slag cement-clayey sand-bentonite (MSB) cutoff wall backfills

Hao-Liang Wu[1,2], Fei Jin[3,4], An-nan Zhou[5], Yan-Jun Du[1]

[1]Jiangsu Key Laboratory of Urban Underground Engineering & Environmental Safety, Institute of Geotechnical Engineering, Southeast University, Nanjing 210096, China.

[2]Department of Civil and Environmental Engineering, Hong Kong University of Science and Technology, Hong Kong SAR, China.

[3] Formerly at School of Engineering, University of Glasgow, Glasgow G12 8QQ, UK.

[4] Currently at School of Engineering, Cardiff University, Cardiff, CF10 3AT, UK.

[5]Civil and Infrastructure Engineering, School of Engineering, Royal Melbourne Institute of Technology (RMIT), Melbourne, Vic 3000, Australia.

[*]Corresponding authors, Email: jinf2@cardiff.ac.uk and duyanjun@seu.edu.cn

Abstract

An innovative cutoff wall backfill consisting of reactive MgO, ground granulated blast furnace slag (GGBS), bentonite and local clayey sand (MSB) was developed recently for land remediation applications. This paper investigates the engineering characteristics (e.g. strength and permeability) and reaction mechanisms of the MSB backfills with different MgO-activated GGBS (i.e., the binder) and bentonite contents. A series of analytical techniques are employed to identify the hydration products in this complex system. The engineering properties are tested via the unconfined compressive strength (UCS) test and flexible-wall permeation test in a triaxial cell. Results show that UCS and dry density decrease with the increasing bentonite content, while the opposite trends are observed when increasing the binder content. The UCS values increase with curing time and become plateaued after ~90 days. Meanwhile, the hydraulic conductivity (k) decreases distinctly with the increase of the binder content and bentonite content. All backfills reach UCS of >100 kPa UCS and $k < 10^{-8}$ m/s at 28 days while curing for 90 days leads to increase of UCS by >1.5 times and reduction of k by nearly one order of magnitude. The major hydration products of MSB backfills are identified as hydrotalcite-like phases (Ht), calcium silicate hydrates (C-S-H), monosulfate (AFm) and portlandite (CH). The hydration products, binding adjacent soil particles, filling pores, together with the swelling of bentonite, contribute to the mechanical performance and impermeability of the backfills.

Keywords: MgO-activated GGBS; cutoff wall; hydration products; engineering properties; reaction mechanisms

1. Introduction

Ground granulated blast furnace slag (GGBS), an industrial by-product of iron production, has been extensively adopted as a replacement of ordinary Portland cement (OPC) (Wang, and Scrivener, 1995). It is known that GGBS imparts significant improvement on the cement and concrete properties including lower heat generation, higher ultimate strength, notably lower hydraulic conductivity, reduced alkalinity, better durability with additional environmental and economic benefits. This has led to the ever-increasing popularity of GGBS in various geotechnical/geoenvironmental applications in recent years (Lam and Jefferis, 2017; Wu et al. 2018a and 2019a; Zheng, et al., 2019; Park et al., 2020). For cutoff walls, partial replacement of OPC with GGBS is employed in several remediation projects (Opdyke and Evans, 2005; Joshi et al., 2009; Li et al., 2020). Findings show that over 60 - 80% OPC could be replaced by GGBS while providing increased strength, reduced bleed and hydraulic conductivity, and higher resistance to sulfate attack to the backfills (Garvin and Hayles, 1999).

Research efforts have been made to understand the activation mechanism and hydration products of GGBS in the presence of various alkalis (Ben Haha et al., 2011; Schöler et al, 2015). The activation process of GGBS begins with the destruction of its chemical bonds (i.e., Si-O, Al-O, and Si-O-Al), followed by the formation of the hydration products such as calcium silicate hydrates (C-S-H) and hydrotalcite ($Mg_6Al_2(OH)_{16}CO_3 \cdot 4H_2O$)-like phases (Ht) via dynamic chemical equilibria and diffusion of reactive species (Krizan 2002; Bernal et al., 2011; Yi et al., 2013 and 2016). Various alkaline earth metal oxides (CaO and MgO) and hydroxides (i.e., $Ca(OH)_2$, $Sr(OH)_2$, and $Ba(OH)_2$) have been found to facilitate the activation of slags (Song, 2000). Particularly, reactive MgO is an emerged novel activator, offering many potential

geomechanical and geoenvironmental benefits over conventional activators (Jin et al. 2015; Du et al. 2016; Wang et al. 2016; Yi et al., 2016). Research reveals that the main hydration products of MgO activated GGBS are C-S-H gel and Ht, resulting in a denser microstructure, improved mechanical performance, as well as excellent pH-buffering and adsorptive capacities, compared to OPC-based binders in heavy metals immobilization (Jin and Al-Tabbaa, 2014a, b and c; Du et al. 2016; Li et al., 2020; Jin and Al-Tabbaa, 2020). Therefore, it is envisaged that MgO-activated GGBS as a binder in cutoff wall applications could provide a significant improvement on the engineering properties with improved long-term durability in land remediation projects.

In previous studies (Wu et al., 2019a and b), laboratory investigations focused on the engineering properties and wetting-drying durability of the novel backfill consisting of MgO-activated GGBS (i.e., the binder), bentonite, and local clayey sand (MSB). Results show that MSB with different mix compositions at 90 days could achieve unconfined compressive strength (UCS) values of 230 - 520 kPa and hydraulic conductivity (k) in clean tap water of 1.1×10^{-10} - 6.3×10^{-10} m/s. It is noted that the k values of MSB backfill using sodium sulfate (30 mmol/L) and lead-zinc (Pb = 0.1 mg/L, Zn = 5 mg/L) solutions as permeant liquids are 1-2 orders of magnitudes lower than those of OPC-based backfills (Wu et al. 2019a). Regarding durability, MSB is marginally more sensitive to a fluctuating groundwater condition (i.e., wet-dry cycles) than OPC-based backfills (Wu et al. 2019b). The UCS values of the MSB backfills decline from 240-560 kPa to 180-420 kPa after 10 wet-dry cycles, though it is still above the commonly adopted design limit ($\geq$ 100 kPa). Despite these promising results, the detailed reaction mechanisms and microstructural characteristics of the MSB mixtures and hence their

91 potential responses to the varying service conditions remain unaddressed. The reaction

92 mechanism of MgO and GGBS blends has been investigated recently (Jin et al., 2015; Park et

93 al., 2020), whereas the interactions between the MgO-activated GGBS, bentonite, and soil

94 remain unresolved. It was reported that the backfill pH and saline cations affected the chemical

95 stability of montmorillonite in bentonite (Jefferis 2012; Du et al. 2020). For example, a high

96 concentration of Ca^{2+} could adversely impact the swelling properties of bentonite and then

97 reduce the hydraulic conductivity (Wu et al. 2019a). Therefore, further studies to reveal the

98 multiscale characteristics of MSB backfills and their interactions with the complex exposure

99 environment in land remediation projects are warranted.

100

101 This paper investigates the evolution of engineering properties, including UCS and hydraulic

102 conductivity, with curing time and different mix compositions of MSB backfills. The

103 geotechnical properties including dry density and void ratio are also reported. Reaction

104 mechanisms and microstructural characteristics of the MSB backfills are revealed via X-ray

105 diffraction (XRD), scanning electron microscopy (SEM), Fourier-transform infrared

106 spectroscopy (FTIR), and Mercury Intrusion Porosimetry (MIP). The hydration products of

107 MSB backfills that consist of a local clayey sand, various dosages of binder and sodium

108 activated calcium-bentonite are probed. The relationship between the engineering properties,

109 hydration products and microstructure of MSB backfills is then discussed.

110

111 **2. Materials and testing program**

112 *2.1 Material*

113 The raw materials used in this study include a local clayey sand, MgO, GGBS and sodium

114 activated calcium-bentonite. The local clayey sand is classified as per ASTM D2487 (2017a)

115 and was collected from the floodplain in Nanjing, China. The basic physicochemical properties

116 of the soil and the chemical compositions of the raw materials measured by X-ray fluorescence

117 can be found in **Wu et al., (2019a)**.

118
119 **Fig. 1 X-ray diffractograms patterns for the sodium activated calcium-bentonite (a) and MgO (b)**
120

121 The commercial powdered sodium activated calcium-bentonite was provided by MuFeng

122 mineral processing plant in Zhenjiang, China. Its specific surface area (SSA) is 378.5 m^2/g, as

123 measured by the nitrogen adsorption method. The MgO (from Jiangsu-Onada Cement Corp.)

124 blended with GGBS (from Nanjing Iron and Steel Group) was used as the binder. The SSA and

125 chemical reactivity of the MgO is 28 m^2/g and 102 s (using the acetic acid test according to

126 Shand (2006)), respectively. It can be categorized as the medium reactivity MgO (Jin and Al-

127 Tabbaa, 2015). The X-ray diffractograms for the sodium activated calcium-bentonite and MgO

128 is shown in **Fig. 1,** which shows the major crystalline phases are montmorillonite and

129 magnesium oxide, respectively. The XRD spectra were obtained using RigakuD/Max-2500

130   spectrometer using a Cu-Kα source with a wavelength of 1.5405 Å. The instrument was

131   operated at 40 kV and 20 mA. A step size of $2\theta = 0.02°$ and a scanning speed of 5 s/step were

132   used.

133

134   *2.2 Specimens*

135   The dosage of the binder and bentonite is 5% - 10% and 5% - 15% by weight of the soil,

136   respectively. The weight ratio of GGBS: MgO in the binder is fixed at 9:1 in this study, which

137   renders adequate strength and lowest hydraulic conductivity as indicated in previous studies

138   (Jin et al. 2015; Wu et al. 2018a and. 2019a). **Table 1** shows the mix proportions of the studied

139   backfills, which are part of the mixes in **(Wu et al., (2019a).** The raw materials, including the

140   soil, bentonite and MgO-activated GGBS were weighted first according to the mix design. A

141   2-L stainless steel mixer was used to blend the dry raw materials at 30 rpm for 5 min. A

142   predetermined amount (to achieve the slump value of 150 ± 5 mm for each mixture according

143   to a preliminary study) of tap water (pH = 6.8; EC = 3.3 μS/cm) was poured into the dry mixture

144   and mixed at 60 rpm for 10 min to achieve homogeneous slurries. The fresh slurries were then

145   cast into cylindrical plastic moulds (Φ50 × H100 mm) to cure for 14-120 days at the

146   temperature of 20 ± 2 °C and relative humidity of 95 ± 1% in sealed plastic boxes until testing.

147

148

Table 1. Mix design of the backfills used in this study (wt%)

Category ID	Raw materials (g)			Slump[a] (mm)	Water content[b], w (%)	Density of soil particle, ρ_s (g/cm³)	Water to binder ratio	Dry density[c], ρ_d (g/cm³)	Void ratio[d], (e)
	Soil	Bentonite	Binder (MgO+GGBS)						
MS5B5	1000	50	50	152	23.9	2.64	5.26	1.42	0.85
MS5B10	1000	100	50	154	33.6	2.65	7.73	1.36	0.93
MS5B15	1000	150	50	152	34.7	2.66	8.33	1.36	0.95
MS10B10	1000	100	100	153	35.4	2.65	4.25	1.37	0.94

MS10B15	1000	150	100	155	36.5	2.66	4.56	1.36	0.94

149 ^a The slump was measured as per ASTM D6103

150 ^b The moisture was measured as per ASTM D2216

151 ^c The dry density was measured as per ASTM D7263

152 ^d Void ratio (e) was determined by $e = \rho_s / \rho_d - 1$, where ρ_s is the soil particle density of backfills and calculated

153 from the raw materials, w is the water content, and ρ_d is the dry density of backfills.

154

155 *2.3 Testing procedure and instruments*

156   UCS was measured in triplicate with a vertical load applied at a constant strain rate of

157 1%/min according to ASTM D4219 (ASTM 2008) after 14, 28, 60, 90 and 120 days of curing.

158 Dry density test was conducted in triplicate as per ASTM D7263 (ASTM 2018b) after each

159 UCS test. The hydraulic conductivity was measured with a flexible-wall permeameter at 22 ±

160 2 °C as detailed in Wu et al., (2019a) for each mixture cured after 28 and 90 days. MS10B10

161 backfill specimens were prepared with freeze-drying methods (dried at -80 °C) for 24 hours for

162 micro-analysis after curing for 90 days. Prior to XRD and FTIR tests, the dry specimens were

163 ground and sieved to < 0.075 mm. FTIR was conducted with a mid-infrared thermo scientific

164 spectrometer (Nicolet 6700) at 4 cm^{-1} scanning resolution. The surface morphology of the

165 MS10B10 backfill was observed by SEM ((LEO1530VP) using 5 kV accelerating voltage. The

166 MIP tests were conducted on freeze-drying samples of MS5B5, MS5B10, MS5B15, MS10B10,

167 MS10B15. As per ASTM D4404 (2010), dry samples were carefully cut from the core of cured

168 samples in approximately 1 cm^3 size and then tested with an Auto Pore IV 9510 mercury

169 intrusion porosimeter at a pressure range from subambient to 413 MPa to determine the pore

170 size distribution.

171 **3. Macroscopic performance: strength and permeability**

172 *3.1 Unconfined compressive strength (UCS)*

173　**Fig. 2** shows the development of UCS, dry density, void ratio and pH of the MSB specimens

174　cured from 14 to 120 days. For each mix composition, a clear trend that UCS increases with

175　increasing curing time is observed. UCS decreases with the increasing bentonite content

176　regardless of the binder content at the same slump value. This can be attributed to the higher

177　water content associated with higher bentonite content to achieve the equivalent workability

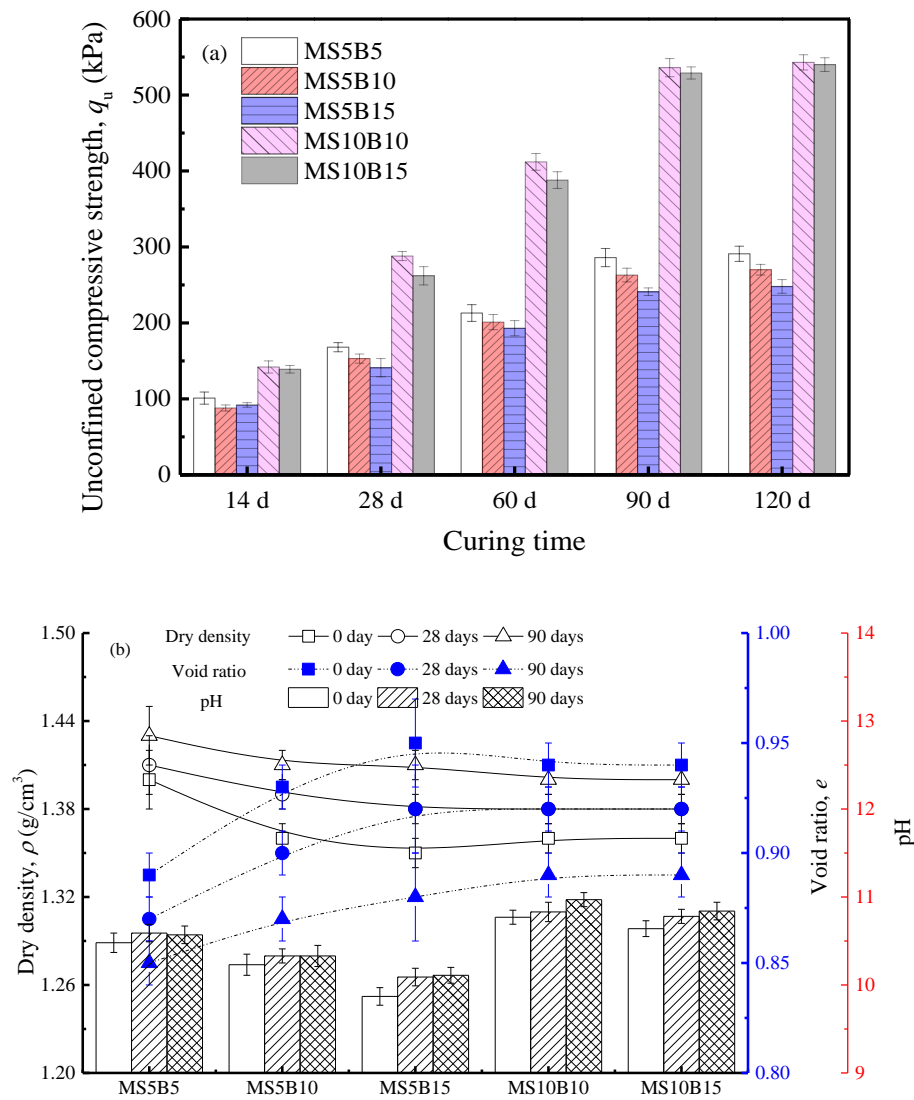178　during the mixing process (**Table 1**).

Fig. 2 Variation of unconfined compressive strength (a) and dry density, void ratio and pH (b) of MSB specimens with curing time (partial data reported in Wu et al., (2019a))

185　At 5% binder content, increasing the bentonite content from 5% to 15% (i.e., comparing

186 MS5B5 with MS5B10 and MS5B15, respectively) is associated with higher initial water

187 content, leading to a slight decrease in dry density and pH value and increase in void ratio,

188 which is consistent with the declined trend of UCS. The ultimate UCS values are approximately

189 doubled when the binder content increased from 5% to 10% at the same bentonite content (i.e.,

190 MS5B10 vs. MS10B10 & MS5B15 vs. MS10B15). The enhanced UCS is mainly due to more

191 binding phases formed when more binder is present, which is also manifested via the elevated

192 pH value as can be see from **Fig. 2 (b)**. The higher pH value facilitates the activation of GGBS

193 and hence producing more hydration products (i.e., C-S-H and Ht) in MSB specimens, leading

194 to higher UCS. On the other hand, there are only marginal changes of the dry density and void

195 ratio since all particles have similar densities and the initial water contents are also close as
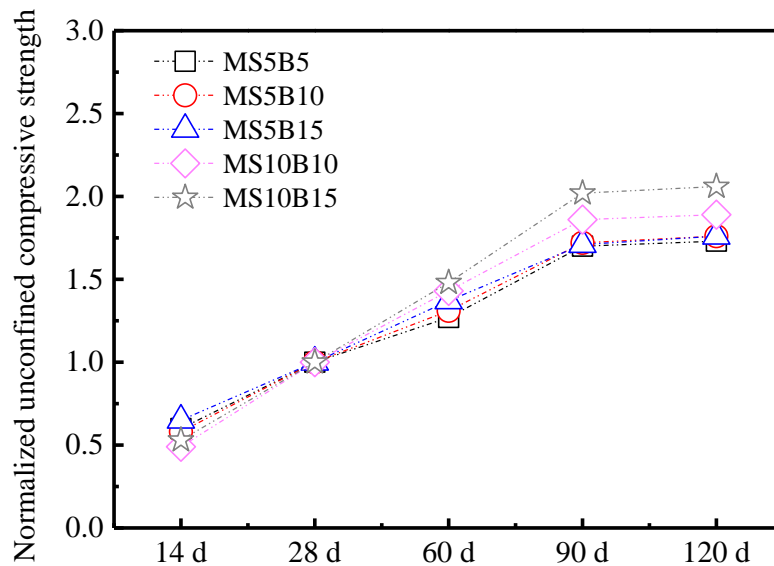
196 shown in Table 1.

197

198
199 **Fig. 3 Normalized unconfined compressive strength at 28-day value of MSB specimens**
200

201 The UCS values are all normalized to the 28-day value for each mixture as shown in **Fig. 3**.

202 The UCS values of the MSB backfills keep increasing after 28 days and plateaue after ~90

203　days. This finding is useful for designing and evaluating the site performance of novel backfill

204　materials as more reasonable curing ages should be adopted for assessment. Particularly, the

205　strength and impermeability development (see Section 4.2) should be modelled properly to

206　account for their long-term performance in order to achieve a more economical design.

207

208　*3.2 Hydraulic conductivity*

209　**Fig. 4** displays the variations of hydraulic conductivity (k) with curing time. The k values of

210　MSB show a pronounced reduction by more than one order of magnitude as curing time

211　increases from 28 to 90 days. The values of k decrease by 52% when the binder content

212　increased from 5% to 10% at 90 days (2.3×10^{-10} m/s for MS5B15 vs. 1.1×10^{-10} m/s for

213　MS10B15). On the other hand, increasing bentonite dosage from 5% to 15% in MSB backfill

214　specimens at 90 days reduces k by ~63% (from 6.3×10^{-10} m/s to 2.3×10^{-10} m/s), which can be

215　attributed to the expanded bentonite particles filling pores. The swelling potential of the

216　bentonite particles are well preserved in the low-pH MgO-activated GGBS cement as indicated

217　in Wu et al., (2019a). It should be noted that the k values of MSB are lower than 1.0×10^{-8} m/s

218　at 28 days as suggested by Evans (1993) and lower than 1.0×10^{-9} m/s at 90 days as required
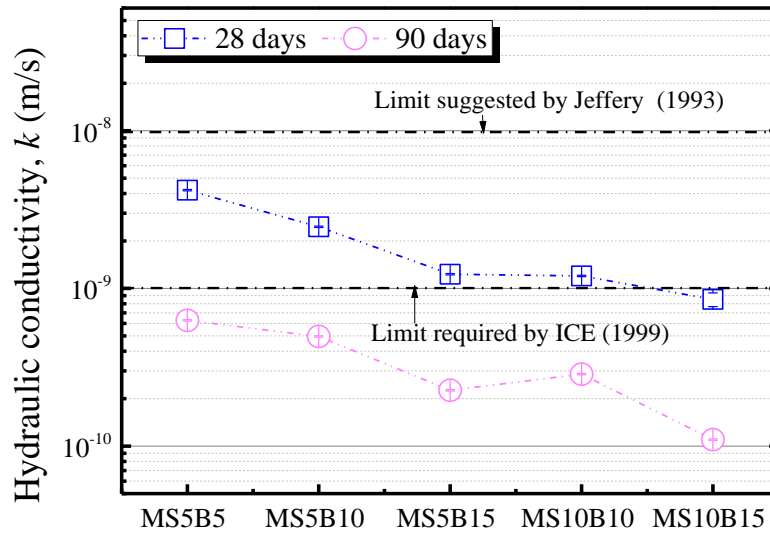
219　by ICE (1999).

Fig. 4 Hydraulic conductivity measured in the flexible wall cells with tap water for each mixture after curing for 28 days and 90 days (partial data reported in Wu et al., (2019a))

4 Microstructural analysis

4.1 X-ray diffraction

The XRD results in **Fig. 5** present the hydration products of the MS10B10 backfills cured for 90 days. The main hydration products are hydrotalcite-like phases (Ht), calcium silicate hydrates (C-S-H), and monosulfate (AFm). The peaks for Ht (identified using $Mg_6Al_2CO_3(OH)_{16} \cdot 4H_2O$, PDF#00-0220700) at $2\theta \approx 12.5°$ and $24.0°$ can be identified, and their intensities increase with the augment in the binder dosage (i.e., MS5B10 vs. MS10B10 and MS5B15 vs. MS10B15) (Jin et al., 2015). The weak Bragg reflections of C-S-H can be detected at $2\theta \approx 23.0°$, $31.6°$ and $37.5°$. The characteristic peak of quartz (SiO_2) in the MSB backfills is detected at $2\theta \approx 21.6°$ from the raw local clayey sand and bentonite (Wu et al., 2019b). The similar magnitude of peaks corresponding to the monosulfate ($Ca_4Al_2(OH)_{12}(S_{0.5}O_2(OH_2)_6)$, PDF# 01-0831289) at $2\theta \approx 9.9°$ and $19.8°$ (Ramachandran et al., 2002) can be observed in all mixes ascribed to the sulfate in the GGBS (**Table 2**). Additionally, the characteristic peak of bentonite (PDF# 00-0030019) is detected at $2\theta \approx 7.48°$, agreeing well

238 with the previous findings (Yang et al., 2018). The peak of calcite (CaCO$_3$, PDF# 00-0030569)

239 (2θ ≈ 29.8°), possibly from the raw materials or the carbonation of the hydration products,

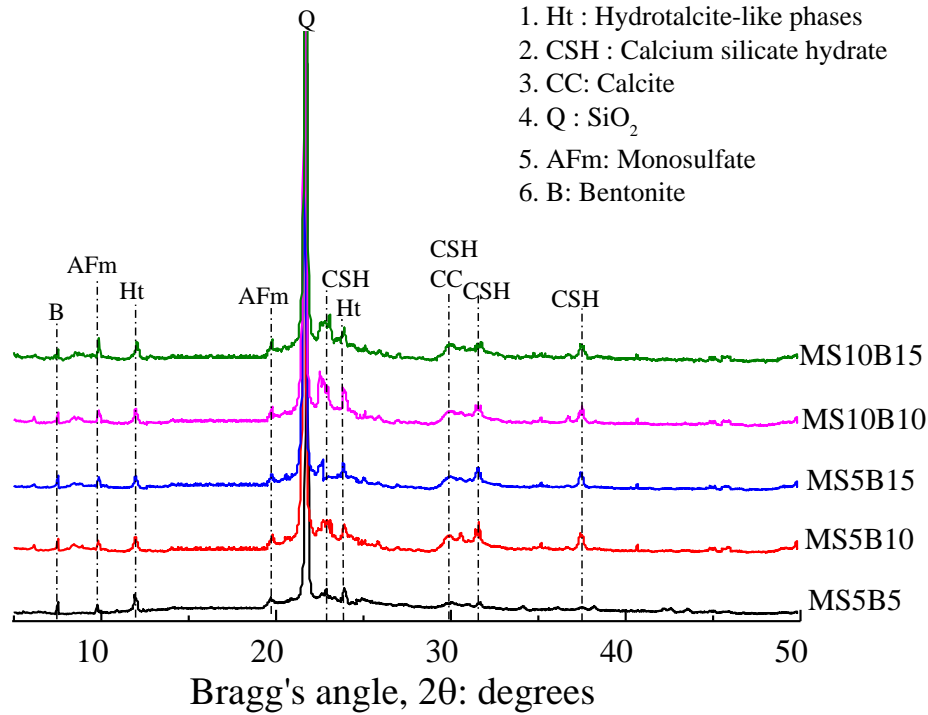240 overlaps with that of C-S-H.

241

242 **Fig. 5 X-ray diffractograms patterns for the 90-day curing of MS10B10 backfills**

243

244 *4.2 Scanning electron microscopy and energy dispersive X-ray spectroscopy*

245 **Fig. 6** shows the microstructure of MS10B10 backfills after 90 days' curing, in which various

246 phases of different morphologies can be observed. It can be seen from **Fig. 6 (a)** that the thin

247 sheet of bentonite particles is characterized by a curly and smooth feature. The large flocculated

248 bentonite and hydration products of MS10B10 backfills fill the pore spaces of soil particles

249 (**Fig. 6 (b)**) and then induced a low hydraulic conductivity (Yang et al., 2018). As shown in

250 **Fig. 6 (c)**, the well-dispersed bentonite particles within the matrix also wrap the soil particles.

251 The well-defined hexagonal platelets of monosulfate (AFm) can be observed in **Fig. 6 (d)**.

13

(a) Thin sheet of bentonite
S4800 15.0kV 9.4mm x20.0k SE(M) 2.00μm

(b) Soil particle — Bentonite and hydration products
0001 15.0kV 4.9mm x100 SE 09/28/2016 500μm

(c) Soil particle — Hydration products — Bentonite
0001 15.0kV 6.2mm x2.00k SE 09/28/2016 20.0μm

(d) AFm $Ca_4Al_2(OH)_{12}(S_{0.5}O_2(OH)_2)_6$
0001 15.0kV 6.3mm x150 SE 09/28/2016 300μm

(e) Fibrous C-S-H gels — GGBS particles
0001 15.0kV 6.7mm x1.00k SE 09/28/2016 50.0μm

(f) Growing hydrotalcite $Mg_6Al_2(OH)_{16}CO_3 \cdot 4H_2O$ — GGBS particles
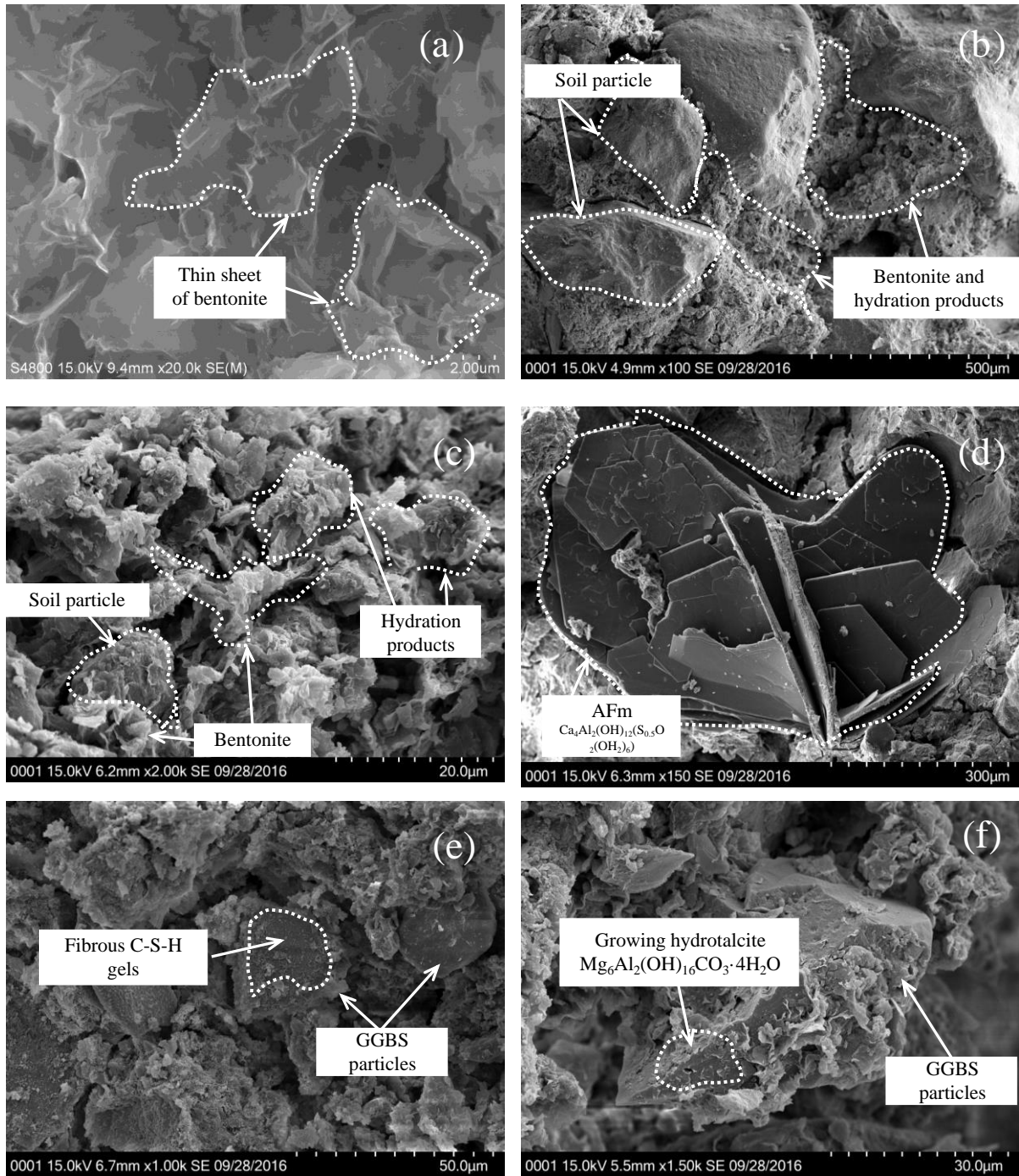0001 15.0kV 5.5mm x1.50k SE 09/28/2016 30.0μm

Fig. 6 SEM images for MS10B10 backfills after 90-day curing

The rough surface of slag particles is undergoing dissolution and then form the fibrous C-S-H (**Fig. 6 (e)**). The dissolution of irregular slag particles also facilitates the formation of Ht as shown in **Fig. 6 (f)**, and the observed morphology is consistent with the previous research (Kovanda et al., 2005). These hydration products, swelling bentonite and unreacted slag

14

259　particles connect to form a dense microstructure, which leads to an increase in strength and

260　decrease in hydraulic conductivity of the MSB backfills.

261

262　*4.3 Fourier-transform infrared spectroscopy*

263　The FTIR spectra of various MSB backfills and the summary of transmittance bands for

264　hydration products of slag-based materials are presented in **Fig. 7** and **Table 2,** respectively.

265　The characteristic peaks of H-O, C-O, Si-O, Al-O and Si-O-X (Mg/Al) bonds can be detected

266　in this study. The characteristic bands of O-H bond and H_2O molecules appear at around 3480

267　cm^{-1} and 1628 cm^{-1} (Fernández-Jiménez and Palomo, 2005), which indicate the presence of

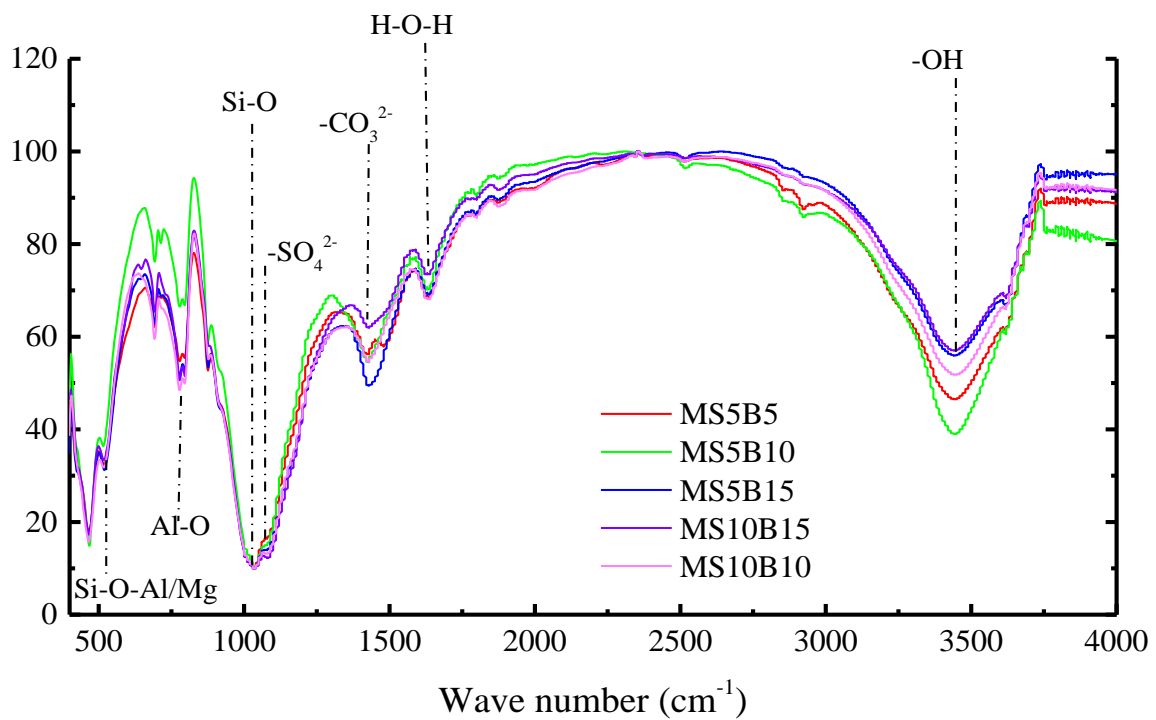268　water as shown in **Fig. 7**.

270　**Fig. 7 Fourier-transform infrared spectra conducted on the 90-day MS10B10 backfill**
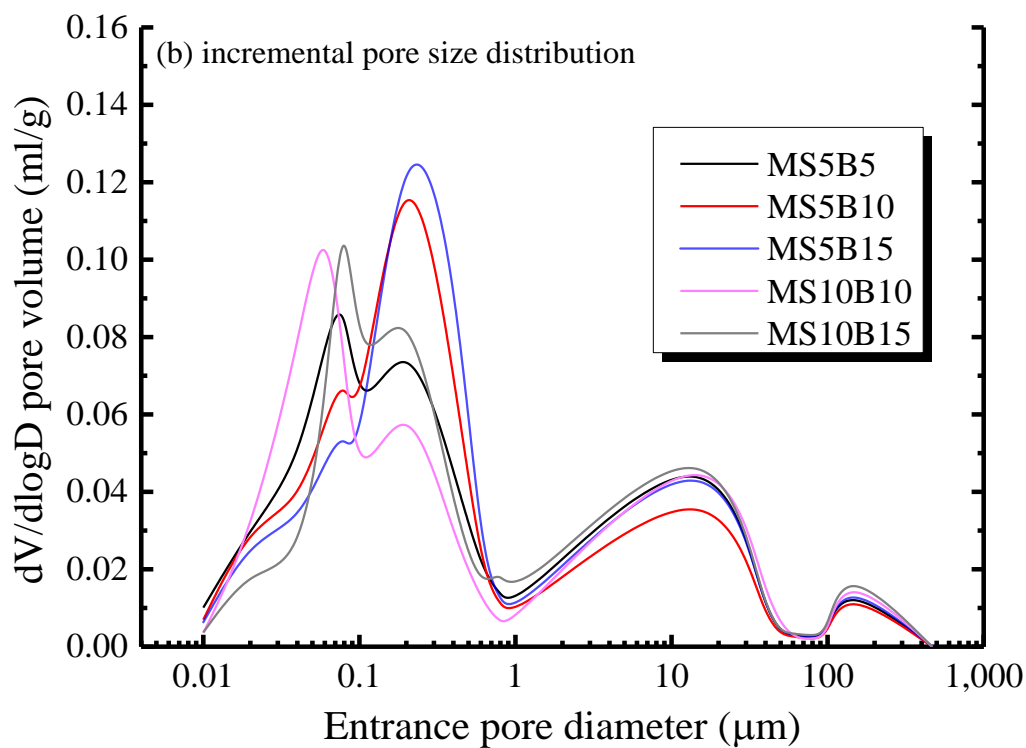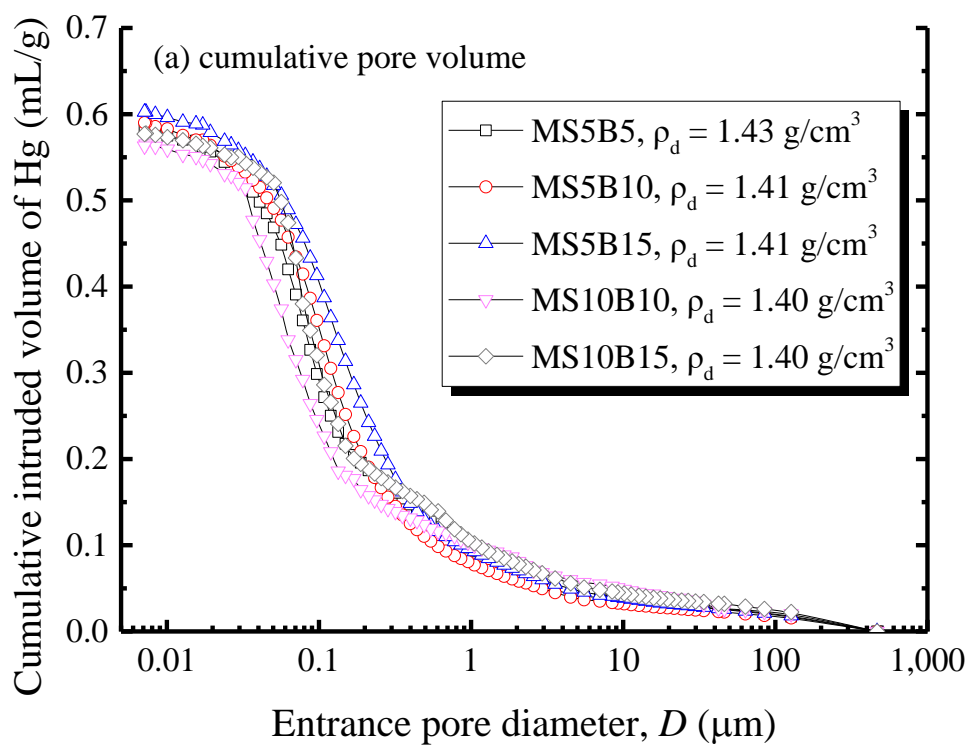
271　The band of $-CO_3^{2-}$ at ~1440 cm^{-1} (Mozgawa and Deja, 2009) confirms the presence of calcite

272　as shown in **Fig. 5**. The slight characteristic $-SO_4^{2-}$ stretching band at ~1057 cm^{-1} (Della et al.

273　2013) indicates the formation of AFm.

15

Table 3. Summary of transmittance bands for hydration products of slag-based materials

Characteristic Bond	Sharp Infrared bands	Reference
Si–O–Al/Mg	670 cm^{-1}	Mozgawa and Deja, 2009
	540 cm^{-1}	Zhang et al., 2007
Al-O	798 cm^{-1}	Zhang et al., 2007
$-SO4^{2-}$	1118 cm^{-1}	Fernández-Jiménez and Palomo, 2005
$-CO_3^{2-}$	1415 cm^{-1}	Mozgawa and Deja, 2009
	712 cm^{-1}	Mozgawa and Deja, 2009
	1450 cm^{-1}	Allahverdi and Najafi Kani, 2009
Si-O	467 cm^{-1}	Zhang et al., 2007
	450 cm^{-1}	Allahverdi and Najafi Kani, 2009
H_2O molecules	1645 cm^{-1}	Fernández-Jiménez and Palomo, 2005
OH$^-$ groups	3450 cm^{-1}	Fernández-Jiménez and Palomo, 2005

4.4 Mercury intrusion porosimetry

Fig. 8 shows the cumulative pore volumes (**Fig. 8 (a)**), incremental pore size distribution (**Fig. 8 (b)**) and proportions of different pore size ranges (**Fig. 8 (c)**) for the MSB backfills at 90 days.

Fig. 8 (a) reveals that increasing bentonite or decreasing binder dosage increases cumulative pore volumes. The cumulative pore volume increases up to 7.9% as the bentonite dosage increases from 5% to 15% at 5% binder content in MSB backfills, i.e., MS5B5 versus MS5B15. It is also observed that the cumulative pore volume of MS10B10 is 12% lower than that of MS5B10 in MSB backfills. It should be noted that increasing bentonite dosage leads to increased initial water content and then increases the pore volume. With the binder content increasing from 5% to 10%, the decreased cumulative pore volume is attributed to the more hydration products (i.e., C-S-H and Ht) generated in the MSB backfills, which is consistent with the UCS trend. Meanwhile, the peak of incremental pore size distribution at 0.2-0.4 μm significantly increases as the bentonite dosage increases from 5% to 15% at 5% binder content (**Fig. 8 (b)**). The increased binder content from 5% to 10% (i.e., MS5B10 *vs*. MS10B10) shifts the peak from 0.2-0.4 μm to 0.04-0.05 μm.
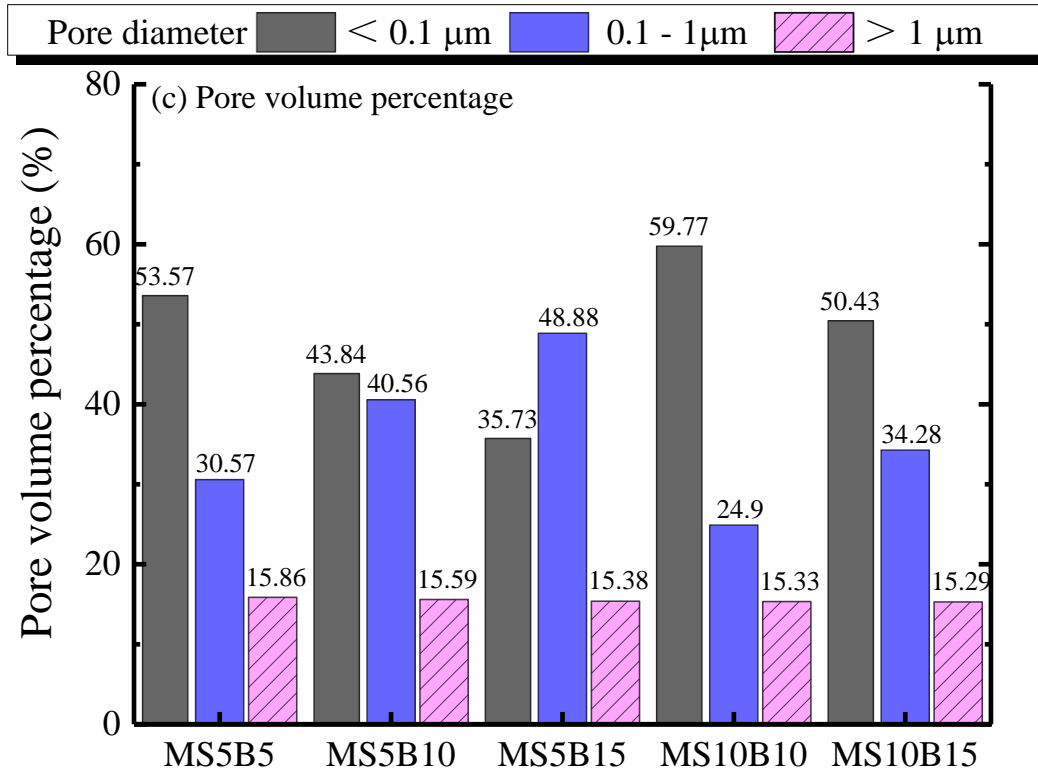
291

292

Fig. 8 Variation of cumulative pore volume (a), incremental pore size distribution and pore volume percentage (c) of 90-days MSB backfills

The three different pore size ranges for the MSB backfills can be classified: >1 μm, 0.1 - 1 μm and < 0.1 μm, respectively, as shown in **Fig. 8 (c)**. At 5% binder dosage, increasing bentonite dosage (MS5B5 vs. MS5B10 vs. MS5B15) results in larger volumes of pores with a diameter of ~ 0.1 - 1 μm, and smaller volumes of < 0.1 μm pores. No significant changes are observed at the pores volume > 1 μm. Moreover, increasing the binder dosage at the same bentonite content (MS5B10 vs. MS10B10 and MS5B15 and MS10B15) significantly decreases the volume of pores with a diameter of 0.1 - 1 μm but increases the volumes of < 0.1 μm pores.

5. Discussion

The reaction products and the microstructural features of the MSB backfills can be summarized as follows. Firstly, MgO particles dissolve in contact with water. The dissolution process of MgO provides an alkaline environment followed by the initial destruction of the covalent bonds

308   (i.e., Si-O, Al-O and Si-O-Al) in GGBS particles (Jin et al., 2015). Meanwhile, bentonite

309   particles once encounter water, start to swell and fill the pore space between the individual soil

310   particles and results in a significant decrease of hydraulic conductivity. In addition, the Ca^{2+}

311   ions leached out from the GGBS and Mg^{2+} replace monovalent cations (i.e., Na^+), which are

312   held on the exchangeable sites of bentonite particles and led to their flocculation. Additionally,

313   the hydroxyl ions could react with the montmorillonite from the bentonite.

314

315   Literature shows that bentonite is relatively stable under a pH value of 12.6 (Ramírez et al.,

316   2002; Sánchez et al., 2006; Omar et al., 2016; Du et al. 2020), which is much higher than the

317   MSB system at pH of 10.2 - 10.8 (Wu et al., 2019a). It is also noted that the swelling

318   performance of sodium-bentonite reaches its peak when bentonite was exposed to alum

319   solution of pH values at 9.8 - 10.6 (Omar et al., 2016). Therefore, excellent impermeability of

320   MSB backfills can be observed in this study due to the preserved swelling potential of bentonite

321   particles as compared to those in the OPC-based backfills. Meanwhile, free ions (Ca^{2+} and

322   Mg^{2+}) released from GGBS and MgO could react with the broken Si-O or Al-O bonds of GGBS

323   to form C-S-H and Ht (**Figs. 5-6**) (with the possible inclusion of Al and sulfate in the structures).

324   The increased binder dosage leads to lower cumulative pore volumes according to MIP and

325   void ratio results (**Figs. 2** and **8**), which are correlated with the increased UCS. Further,

326   increasing bentonite dosage leads to increased initial water content and then increases the pore

327   volume (measured at the dry state by MIP). Here a distinction must be made regarding the pore

328   volume at wet and dry states. At the wet state, increasing bentonite dosage can increase

329   swelling volume and may reduce the pore volume and hydraulic conductivity. The monosulfate

330   phase (**Figs. 5**) is produced from the relatively small amount of sulfate content in GGBS (and

331 possibly from the local soil), which also could contribute to filling the large-sized pores and

332 converting them to relatively small-sized pores (**Fig. 8**). In summary, the improved UCS and

333 impermeability of the MSB system can be attributed to the binding and pore filling effect of

334 the various hydration products as well as the swelling bentonite particles (**Figs. 4 & 8**).

335

336 Previous studies extensively investigated the reaction mechanisms of the MgO-GGBS binder,

337 showing its unique features of low-pH, high strength and low permeability in the long term (>

338 90 days) and superior durability. The present work focuses on the engineering properties and

339 reaction mechanisms of MgO-GGBS-bentonite-soil mixtures targeting cutoff wall applications.

340 The results apparently show that this novel backfill material satisfies both strength and

341 permeability requirements at 28 days and much enhanced performance is demonstrated at 90

342 days. The preserved bentonite observed at 90 days shows the advantages of using low-pH

343 MgO-GGBS in vertical cutoff walls and provides insights into developing more durable cutoff

344 wall backfills. Moreover, the use of site soil proves to be successful in this study which would

345 contribute to more economical cutoff wall backfills in the real applications. In order to promote

346 the design/adoption of more sustainable and durable cutoff wall materials, more work is desired

347 regarding contaminant transport modeling, contaminated site soil utilization and full-scale field

348 trials. Besides, more fundamental research is warranted such as determining the reaction

349 kinetics of the MgO-GGBS-bentonite system under different underground conditions and

350 modification of bentonite to enhance its stability and sorption capacity.

351 **6. Conclusions**

352 The multiscale engineering characteristics, hydration products and microstructural

353 characteristics of MSB backfills with different dosages of MgO-activated GGBS (i.e., the

354 binder) and bentonite are evaluated in this study. The following conclusions can be drawn:

355 (1) The strength and hydraulic conductivity of MSB backfills can achieve ~520 kPa and

356 1.1×10^{-10} m/s after curing 90 days, respectively. The strength and dry density increase with the

357 increase of the binder content and decrease of bentonite dosage. Meanwhile, the hydraulic

358 conductivity can be lowered by 52% and 63% as the binder increased from 5% to 10% and

359 bentonite dosage increased from 5% to 15%, respectively.

360 (2) The engineering properties of MSB backfills improved significantly from 28 to 90

361 days. For geotechnical practices especially the cutoff walls, it is important to evaluate the

362 performance of MSB backfills properly taking into account of the evolution of the strength and

363 impermeability over the long term to enable more efficient and economical design.

364 (3) The hydration products of MSB backfills include hydrotalcite-like phases, calcium

365 silicate hydrates, monosulfate, and portlandite. Furthermore, the increased binder dosage leads

366 to lower cumulative pore volume, which agrees well with the trends observed in strength and

367 hydraulic conductivity development.

368 (4) The bentonite particles are relatively stable in the MSB system. The hydration products,

369 binding the adjacent soil particles and filling the pores in between, together with the swelling

370 of bentonite, contribute to the enhancement of the mechanical performance and impermeability

371 of the MSB backfills.

372

References

[1] Allahverdi, A., & Najafi Kani, E. 2009. Construction wastes as raw materials for geopolymer binders. International Journal of Civil Engineering, 7(3), 154-160.

[2] ASTM. 2008. Standard test method for unconfined compressive strength index of chemical-grouted soils. ASTM D4219. West Conshohocken, PA, USA: ASTM International.

[3] ASTM. 2010a. Standard Test Methods for Laboratory Determination of Water (Moisture) Content of Soil and Rock by Mass. ASTM D2216. West Conshohocken, PA, USA: ASTM International.

[4] ASTM. 2010b. Standard Test Methods for Liquid Limit, Plastic Limit, and Plasticity Index of Soils. ASTM D4318, West Conshohocken, PA, USA: ASTM International.

[5] ASTM, 2010c. Standard Test Method for Measuring the Exchange Complex and Cation Exchange Capacity of Inorganic Fine-Grained Soils. ASTM D7053, West Conshohocken, PA, USA: ASTM International.

[6] ASTM, 2010d. Standard test method for determination of pore volume and pore volume distribution of soil and rock by mercury intrusion porosimetry. ASTM D4404. West Conshohocken, PA, USA: ASTM International.

[7] ASTM. 2016. Standard test methods for measurement of hydraulic conductivity of

397   saturated porous materials using a flexible wall permeameter. ASTM D5084. West

398   Conshohocken, PA, USA: ASTM International.

399   [8] ASTM. 2017a. Standard Practice for Classification of Soils for Engineering Purposes

400   (Unified Soil Classification System). ASTM D2487. West Conshohocken, PA, USA:

401   ASTM International.

402   [9] ASTM. 2017b. Standard Test Method for Flow Consistency of Controlled Low Strength

403   Material (CLSM). ASTM D6103. West Conshohocken, PA, USA: ASTM International.

404   [10] ASTM. 2018a. Standard Test Method for pH of Soils. ASTM D4972. West Conshohocken,

405   PA, USA: ASTM International.

406   [11] ASTM. 2018b. Standard test methods for laboratory determination of density (unit weight)

407   of soil specimens. ASTM D7263. West Conshohocken, PA, USA: ASTM International.

408   [12] Ben Haha, M., Lothenbach, B., Le Saout, G., and Winnefeld, F. 2011. Influence of slag

409   chemistry on the hydration of alkali-activated blast-furnace slag - Part I: Effect of MgO.

410   Cement and Concrete Research, 41(9): 955–963.

411   [13] Bernal, S. A., Provis, J. L., Rose, V., & De Gutierrez, R. M. 2011. Evolution of binder

412   structure in sodium silicate-activated slag-metakaolin blends. Cement and Concrete

413   Composites, 33(1), 46-54.

414   [14] Cerato, A. B., and Lutenegger, A. J. 2002. Determination of surface area of fine-grained

415   soils by the ethylene glycol monoethyl ether (EGME) method. Geotechnical Testing

416   Journal, 25(3), 315-321.

417   [15] Della Ventura, G., Ventruti, G., Bellatreccia, F., Scordari, F., & Guidi, M. C. 2013. FTIR

418   transmission spectroscopy of sideronatrite, a sodium-iron hydrous sulfate. Mineralogical

419 Magazine, 77(4), 499-507.

420 [16] Du, J., Zhou, A., Lin, X., Bu, Y. and Kodikara, J., 2020. Revealing Expansion Mechanism

421 of Cement Stabilized Expansive Soil with Different Interlayer Cations through Molecular

422 Dynamics Simulation. The Journal of Physical Chemistry C, 124(27), 14672–14684.

423 https:// doi.org/10.1021/acs.jpcc.0c03376

424 [17] Du, Y. J., Bo, Y. L., Jin, F., and Liu, C. Y. 2016. Durability of reactive magnesia-activated

425 slag-stabilized low plasticity clay subjected to drying–wetting cycle. European Journal of

426 Environmental and Civil Engineering, 20(2), 215-230.

427 [18] Evans, J.C. 1993. Vertical cutoff walls. In Geotechnical Practice for Waste Disposal;

428 Daniel, D.E., Ed.; Chapman & Hall: London, UK, pp. 430–454.

429 [19] Fernández-Jiménez, A., & Palomo, A. 2005. Composition and microstructure of alkali

430 activated fly ash binder: Effect of the activator. Cement and concrete research, 35(10),

431 1984-1992.

432 [20] Garvin, S. L., & Hayles, C. S. 1999. The chemical compatibility of cement–bentonite cut-

433 off wall material. Construction and Building Materials, 13(6), 329-341.

434 [21] Heikal, M., Aiad, I., Shoaib, M. M., & El-Didamony, H. 2001. Physico-chemical

435 characteristics of some polymer cement composites. Materials chemistry and physics,

436 71(1), 76-83.

437 [22] ICE (Institution of Civil Engineers). 1999. Specification for the construction of slurry

438 trench cut-off walls as barriers to pollution migration. London: Thomas Telford.

439 [23] Jin, F., Gu, K., and Al-Tabbaa, A. 2014a. Strength and drying shrinkage of reactive MgO

440 modified alkali-activated slag paste. Construction and Building Materials, 51, 395–404.

441   [24] Jin, F., and Al-Tabbaa, A. 2014b. Characterisation of different commercial reactive

442   magnesia. Advances in Cement Research, 26(2), 101-113..

443   [25] Jin, F., and Al-Tabbaa, A. 2014c. Evaluation of novel reactive MgO activated slag binder

444   for the immobilization of lead and zinc. Chemosphere, 117: 285-294.

445   [26] Jin, F., Gu, K. and Al-Tabbaa, A. 2015. Strength and hydration properties of reactive MgO-

446   activated ground granulated blastfurnace slag paste. Cement and Concrete Composites, 57,

447   8-16.

448   [27] Jin, F., and Al-Tabbaa, A. 2020. Magnesia in alkali activated cements. Magnesia Cements,

449   Elsevier, Oxford, United Kingdom, pp. 213-241.

450   [28] Joshi, K., Kechavarzi, C., Sutherland, K., Ng, M. Y. A., Soga, K., and Tedd, P. 2009.

451   Laboratory and in situ tests for long-term hydraulic conductivity of a cement-bentonite

452   cutoff wall. Journal of Geotechnical and Geoenvironmental Engineering, 136(4), 562-572.

453   [29] Kovanda, F., Koloušek, D., Cílová, Z., & Hulínský, V. 2005. Crystallization of synthetic

454   hydrotalcite under hydrothermal conditions. Applied clay science, 28(1-4), 101-109.

455   [30] Krizan, D., & Zivanovic, B. (2002). Effects of dosage and modulus of water glass on early

456   hydration of alkali–slag cements. Cement and Concrete Research, 32(8), 1181-1188.

457   [31] Lam, C., and S. A. Jefferis. 2017. Polymer Support Fluids in Civil Engineering, ICE

458   Publishing, One Great George Street, Thomas Telford Limited, London.

459   [32] Li, W., Yi, Y., & Puppala, A. J. 2020. Suppressing Ettringite-Induced Swelling of Gypseous

460   Soil by Using Magnesia-Activated Ground Granulated Blast-Furnace Slag. Journal of

461   Geotechnical and Geoenvironmental Engineering, 146(7), 06020008.

462   [33] Lodeiro, I. G., Fernández-Jimenez, A., Palomo, A., & Macphee, D. E. 2010. Effect on fresh

463   CSH gels of the simultaneous addition of alkali and aluminium. Cement and Concrete

464   Research, 40(1), 27-32.

465 [34] Mozgawa, W., & Deja, J. 2009. Spectroscopic studies of alkaline activated slag

466   geopolymers. Journal of Molecular Structure, 924, 434-441.

467 [35] Omar, M., Shanableh, A., & Al Zaylaie, M. (2016). Modification of the swelling

468   characteristics and phosphorus retention of bentonite clay using alum. Soils and

469   Foundations, 56(5), 861-868.

470 [36] Opdyke, S. M., and Evans, J. C. 2005. Slag-cement-bentonite slurry walls. Journal of

471   Geotechnical and Geoenvironmental Engineering, 131(6), 673-681.

472 [37] Park, S., Park, H. M., Yoon, H. N., Seo, J., Yang, C. M., Provis, J. L., & Yang, B. 2020.

473   Hydration kinetics and products of MgO-activated blast furnace slag. Construction and

474   Building Materials, 249, 118700.

475 [38] Ramírez, S., Cuevas, J., Vigil, R., & Leguey, S. 2002. Hydrothermal alteration of "La

476   Serrata" bentonite (Almeria, Spain) by alkaline solutions. Applied Clay Science, 21(5-6),

477   257-269.

478 [39] Sánchez, L., Cuevas, J., Ramírez, S., De León, D. R., Fernández, R., Villa, R. V. D., &

479   Leguey, S. 2006. Reaction kinetics of FEBEX bentonite in hyperalkaline conditions

480   resembling the cement–bentonite interface. Applied Clay Science, 33(2), 125-141.

481 [40] Schöler, A., Lothenbach, B., Winnefeld, F., & Zajac, M. 2015. Hydration of quaternary

482   Portland cement blends containing blast-furnace slag, siliceous fly ash and limestone

483   powder. Cement and Concrete Composites, 55, 374-382.

484 [41] Shand, M. A. 2006. The chemistry and technology of magnesia, John Wiley & Sons.

485   [42] Song, S., Sohn, D., Jennings, H. M., & Mason, T. O. 2000. Hydration of alkali-activated

486   ground granulated blast furnace slag. Journal of materials science, 35(1), 249-257.

487   [43] Wang, F., Jin, F., Shen, Z., & Al-Tabbaa, A. 2016. Three-year performance of in-situ mass

488   stabilised contaminated site soils using MgO-bearing binders. Journal of Hazardous

489   Materials, 318, 302-307.

490   [44] Wang, S.D., and Scrivener, K.L. 1995. Hydration products of alkali activated slag cement.

491   Cement and Concrete Research, 25(3): 561–571.

492   [45] Wu, H. L., Jin, F., Bo, Y. L., Du, Y. J., and Zheng, J. X. 2018a. Leaching and

493   microstructural properties of lead contaminated kaolin stabilized by GGBS-MgO in semi-

494   dynamic leaching tests. Construction and Building Materials, 172, 626-634.

495   [46] Wu, H. L., Zhang, D., Ellis, B. R., and Li, V. C. 2018b. Development of reactive MgO-

496   based Engineered Cementitious Composite (ECC) through accelerated carbonation curing.

497   Construction and Building Materials, 191, 23-31.

498   [47] Wu, H. L., Jin, F., Ni, J. and Du, Y. J. 2019a. Engineering properties of vertical cutoff

499   walls consisting of reactive magnesia-activated slag and bentonite: workability, strength

500   and hydraulic conductivity. Journal of Materials in Civil Engineering.

501   [48] Wu, H. L., Jin, F., & Du, Y. J. 2019b. Influence of wet-dry cycles on vertical cutoff walls

502   made of reactive magnesia-slag-bentonite-soil mixtures. Journal of Zhejiang University-

503   SCIENCE A, 20(12), 948-960.

504   [49] Wu, H. L., Du, Y. J., Yu, J., Yang, Y. L., & Li, V. C. 2020. Hydraulic conductivity and

505   self-healing performance of Engineered Cementitious Composites exposed to Acid Mine

506   Drainage. Science of The Total Environment, 716, 137095.

507 [50] Yang, Y. L., Reddy, K. R., Du, Y. J., & Fan, R. D. 2018. Sodium hexametaphosphate

508   (SHMP)-amended calcium bentonite for slurry trench cutoff walls: workability and

509   microstructure characteristics. Canadian Geotechnical Journal, 55(4), 528-537.

510 [51] Yi, Y., Liska, M., Al-Tabbaa. 2013. A. Properties of two model soils stabilized with

511   different blends and contents of GGBS, MgO, lime, and PC. Journal of Materials in Civil

512   Engineering, 26, 267-274

513 [52] Yi, Y., Liska, M., Jin, F., & Al-Tabbaa, A. 2016. Mechanism of reactive magnesia–ground

514   granulated blastfurnace slag (GGBS) soil stabilization. Canadian Geotechnical Journal,

515   53(5), 773-782.

516 [53] Zhang Y.S., Sun W., Chen Q.L., C., & Chen L. 2007. Synthesis and heavy metal

517   immobilization behaviors of slag based geopolymer. Journal of hazardous materials,

518   143(1-2), 206-213.

519 [54] Zheng, J., Sun, X., Guo, L., Zhang, S., & Chen, J. 2019. Strength and hydration products

520   of cemented paste backfill from sulphide-rich tailings using reactive MgO-activated slag

521   as a binder. Construction and Building Materials, 203, 111-119.